

ASASSN-15lh: A SUPERLUMINOUS ULTRAVIOLET REBRIGHTENING OBSERVED BY SWIFT AND HUBBLE*

PETER J. BROWN¹, YI YANG¹, JEFF COOKE², MELANIE OLAES³, ROBERT M. QUIMBY^{3,4},
DIETRICH BAADE⁵, NEIL GEHRELS⁶, PETER HOEFLICH⁷, JUSTYN MAUND⁸,
JEREMY MOULD², LIFAN WANG¹, & J. CRAIG WHEELER⁹

Draft version August 12, 2016

ABSTRACT

We present and discuss ultraviolet and optical photometry from the Ultraviolet/Optical Telescope and X-ray limits from the X-Ray Telescope on Swift and imaging polarimetry and ultraviolet/optical spectroscopy with the Hubble Space Telescope of ASASSN-15lh. It has been classified as a hydrogen-poor superluminous supernova (SLSN I) more luminous than any other supernova observed. ASASSN-15lh is not detected in the X-rays in individual or coadded observations. From the polarimetry we determine that the explosion was only mildly asymmetric. We find the flux of ASASSN-15lh to increase strongly into the ultraviolet, with a ultraviolet luminosity a hundred times greater than the hydrogen-rich, ultraviolet-bright SLSN II SN 2008es. We find objects as bright as ASASSN-15lh are easily detectable beyond redshifts of ~ 4 with the single-visit depths planned for the Large Synoptic Survey Telescope. Deep near-infrared surveys could detect such objects past a redshift of ~ 20 enabling a probe of the earliest star formation. A late rebrightening – most prominent at shorter wavelengths – is seen about two months after the peak brightness, which is itself as bright as a superluminous supernova. The ultraviolet spectra during the rebrightening are dominated by the continuum without the broad absorption or emission lines seen in SLSNe or tidal disruption events and the early optical spectra of ASASSN-15lh. Our spectra show no strong hydrogen emission, showing only Ly α absorption near the redshift previously found by optical absorption lines of the presumed host. The properties of ASASSN-15lh are extreme when compared to either SLSNe or tidal disruption events.

Subject headings: supernovae: general — supernovae: individual (ASASSN-15lh, SN2015L, SN2008es)
— ultraviolet: general

1. INTRODUCTION

Superluminous supernovae (SLSNe) are a recently discovered class of supernovae that are up to 50 times more luminous than Type Ia supernovae (Quimby et al. 2007; Smith et al. 2007; Quimby et al. 2011). Their observed behavior is varied, and the well-studied examples have been further subdivided (see e.g. Gal-Yam 2012 for a review). Analogous to classical supernova typing, SLSNe I have no hydrogen in their spectra and they may be

related to Type Ic supernovae (Pastorello et al. 2010), whereas SLSN II are hydrogen rich. Mechanisms that power normal supernovae, such as the radioactive decay of ^{56}Ni and gravitational collapse, cannot reproduce their total integrated energy and light curve rise and fade rates (Sukhbold & Woosley 2016). Inserra et al. (2013) and Nicholl et al. (2013, 2014) find that energy deposition by the spin-down of a magnetic neutron star (a magnetar; Kasen & Bildsten 2010; Woosley 2010; Dessart et al. 2012) can explain the light curve behavior of many SLSNe I, yet the models are not unique and require parameters tuned to the observations. Interaction with pre-expelled circumstellar material is believed to drive the high energy and emission lines observed for SLSNe II (Smith et al. 2007; Chatzopoulos et al. 2011, 2013). For the slowest evolving SLSNe, Gal-Yam (2012); Kozyreva et al. (2014) suggested a SLSN R class powered by radioactive decay of several solar masses of Ni, as was argued for SN 2007bi (Gal-Yam et al. 2009). Their progenitors are predicted to be extremely massive (~ 140 – $260 M_{\odot}$) and result in a pair-instability supernova explosion (PISN). Objects similar to SN 2007bi but with better data, however, are not consistent with the pair-instability model and suggest magnetars as the likely explosion mechanism (Nicholl et al. 2013). Some SLSNe exhibit double peaks in their light curves which may be a signature of pulsational PISNe (Leloudas et al. 2012; Cooke et al. 2012; Nicholl & Smartt 2016). One object, iPTF13ehe, exhibits characteristics of a large radioactive nickel mass and magnetar heating, as well as late time circumstellar interaction (Yan et al. 2015; Wang et al.

*Based on observations with the NASA/ESA Hubble Space Telescope obtained at the Space Telescope Science Institute, which is operated by the Association of Universities for Research in Astronomy, Incorporated, under NASA contract NAS5-26555.

¹ George P. and Cynthia Woods Mitchell Institute for Fundamental Physics & Astronomy, Texas A. & M. University, Department of Physics and Astronomy, 4242 TAMU, College Station, TX 77843, USA

² Centre for Astrophysics & Supercomputing, Swinburne University, Hawthorn VIC 3122, Australia

³ Department of Astronomy, San Diego State University, San Diego, CA 92182, USA

⁴ Kavli IPMU (WPI), UTIAS, The University of Tokyo, Kashiwa, Chiba 277-8583, Japan

⁵ European Organisation for Astronomical Research in the Southern Hemisphere (ESO), Karl-Schwarzschild-Str. 2, 85748 Garching b. München, Germany

⁶ NASA Goddard Space Flight Center, Greenbelt, MD 20771, USA

⁷ Department of Physics, Florida State University, Tallahassee, FL 32306, USA

⁸ Department of Physics and Astronomy F39 Hicks Building, Hounsfield Road Sheffield, S3 7RH, United Kingdom

⁹ Department of Astronomy, University of Texas at Austin, Austin, TX 78712, USA

2015).

In addition to their higher optical luminosity, an important difference between SLSNe and SNe Ia is their UV luminosity. SNe Ia exhibit a sharp drop in flux at wavelengths below 3000 Å. This drop has been exploited to identify SNe Ia in the Hubble Deep Field (Riess et al. 2004) but makes it hard to observe higher redshift SNe in the optical. It imposes a de-facto redshift limit of ~ 1.7 beyond which optical filters cover the intrinsically faint UV region. In contrast, SLSNe show significant UV flux. SLSNe I do not show the strong metal line blanketing which suppresses the UV flux in other type I SNe. SLSNe II show a very strong rise in flux to shorter wavelengths, similar to the hot photospheres of the classical hydrogen-dominated SNe II. For the earliest observations of SN 2008es ($z=0.205$) the wavelength of the peak flux was shortward of the Swift UV observations (rest wavelength of ~ 1500 Å; Gezari et al. 2009). Thus UV observations are important for measuring the total luminosity and constraining the temperature. The lack of UV data can make it hard to compare the luminosities of SLSNe (Chomiuk et al. 2011). From a purely observational standpoint, the high UV flux makes it much easier to detect these SNe at large distances because the UV flux redshifting into the optical bands helps rather than hurts. The current most distant SLSN was discovered at $z=3.9$ (Cooke et al. 2012). Finally, as astrophysical tools, SLSNe can be used as backlights to probe absorption from the interstellar medium similar to quasars and GRBs (Berger et al. 2012).

While we focus on the SLSN scenario, we will also discuss how the observations compare to those of tidal disruption events (TDEs) –luminous, hot transients resulting from the tidal disruption of a star by a previously inactive galactic nucleus (Rees 1988; Loeb & Ulmer 1997).

The luminous ASASSN-15lh (Dong et al. 2016a) was discovered by the All Sky Automated Survey for SuperNovae (ASASSN) and announced as a hydrogen-poor SLSN with rest-frame u-band absolute magnitude of -23.5 (AB system) and extremely blue UV colors (Dong et al. 2015). The unprecedented luminosity challenged many of the adopted models for SLSNe (Dong et al. 2016a). The unknown mechanism powering these explosions and the extreme nature of ASASSN-15lh make multi-wavelength data of great importance to constraining possible models. In Section 2 we present the Swift/UVOT and HST observations and briefly outline the calibration and reduction. In Section 3 we describe the light curve, implied symmetry from the polarimetry, spectral shape, UV spectrum, and the X-ray limits. In Section 4 we discuss the nature of the rebrightening, some similarities and differences to TDEs, and the detectability of such objects to very high redshifts. We summarize in Section 5.

2. OBSERVATIONS OF ASASSN-15lh

ASASSN-15lh, was discovered by the All Sky Automated Survey for SuperNovae (ASAS-SN) on UT 2015-06-14.25 (MJD 57187.25) and announced June 16 (Nicholls et al. 2015). It was present near the detection limit of $V \sim 17.3$ on May 18.32 and not detected on May 15.33 or before to a limit of $V \sim 17.3$. UV observations with the Swift/Ultraviolet Optical Telescope (UVOT; Roming et al. 2005) showed it to be extremely

blue (Dong et al. 2015). Dong et al. (2015) also reported a spectral classification on 2015 July 8, describing a blue mostly featureless continuum with broad OII lines similar to hydrogen-poor SLSNe I. They determined a redshift of $z=0.2326$ from MgII absorption lines, implying an absolute magnitude in the rest-frame u band of -23.5 (AB system). A detailed description of the early UV and optical properties is given by Dong et al. (2016a). Fitting a parabola to the V-band data yields the epoch of maximum light in the optical to be 2015 June 05 (MJD 57178.5).

2.1. Swift Ultraviolet Optical Telescope and X-Ray Telescope Observations

Observations with Swift began 2015 June 24 00:37:49 (MJD 57197). The early UVOT data were reported by Dong et al. (2016b). Following the announcement of the superluminous nature of ASASSN-15lh (Dong et al. 2015) we triggered our Swift Guest Investigator programs “Ultraviolet Properties of Superluminous Supernovae over Ten Billion Years” (PI: Brown) to obtain UV/optical photometry with Swift/UVOT and “Late-Time X-Rays from Superluminous Supernovae: How Hard Could it Be?” (PI: Quimby). We have reduced all of the data obtained through 2016 Apr 1. The reduction utilizes the same routines as the Swift Optical/Ultraviolet Supernova Archive (SOUSA; Brown et al. 2014). One change is that the time-dependent sensitivity correction of Breeveld et al. (2011) has been updated¹⁰. No attempt has been made to subtract off the count rates of the underlying galaxy, only expected to be significant at the faintest epochs of our optical filters Dong et al. (2016a). We use the revised Swift/Vega system and AB zeropoints of Breeveld et al. (2011). The Swift/UVOT photometry on the Swift/Vega system is given in Table 1 and displayed in the AB system (for appearance reasons) in Figure 1.

One might be concerned about the effect of the optical tails of the uvw2 and uvw1 filters (sometimes referred to as the “red leaks”) which still have 1/1000 of the peak transmission all the way to 5000 Å (see Breeveld et al. 2011 and Brown et al. 2010 for graphical descriptions of the revised filter throughput curves). To estimate the contribution from the optical tails, we compare the count rates to those expected through synthetic filters similar to uvw2 and uvw1 but cutting off sharply to zero throughput at 2500 and 3300 Å (Brown et al. 2010). Using a blackbody spectrum corresponding to 16,000 K (the hottest estimated below), the counts coming from the redder portion correspond to 12% and 3 % of the total in the uvw2 and uvw1 filters, respectively. Using a blackbody spectrum corresponding to 10,770 K (the coolest estimated below), the extra counts coming from the redder portion correspond to 20% and 5 % of the total in the uvw2 and uvw1 filters, respectively. Thus the contribution from the red tails increases as the SN reddens, but never contributes a large fraction of the counts. The wavelengths beyond which are considered to be part of a red leak (as opposed to just the long wavelength edge of the filter) can be arbitrary and require a spectral model as well as the filter curves to quantify.

¹⁰ <http://heasarc.gsfc.nasa.gov/docs/heasarc/caldb/swift/docs/uvot/uvot/>

Even if the red leak contributed a significant fraction of the observed count rate in the UV filters, the analysis below takes the red leaks into account. For example, blackbody fits are performed by comparing the observed count rates to those predicted from blackbody spectra through the whole filter. Brown et al. (2016, AJ accepted) give a detailed description of issues involved with the conversion of Swift/UVOT broadband measurements into monochromatic flux densities for the generation of spectral energy distributions and bolometric light curves.

Observations with the X-Ray Telescope (Burrows et al. 2005) were obtained simultaneously with UVOT. Count rates were extracted as follows: Source regions were selected at a 5 pixel radius according to the in-flight calibration of the Swift XRT point spread function (Moretti et al. 2005). Similarly, the background region radius was selected with a 10 pixel inner radius and a 100 pixel outer radius. Counts were extracted using the HEASoft tool `xselect` from each event file to determine total counts in a specified region and exposure time. Where observations were taken within 14.4 minutes of each other, the data were combined and the limits recalculated.

Limits for the source were determined using the Bayesian method outlined in Kraft et al. (1991), constructing a posterior probability distribution function based on N counts in the source region and B expected background counts. Minimum and maximum source limits were then taken at a given confidence limit. Table 2 and Figure 2 provide three sigma limits in unabsorbed flux and luminosity for each of the individual epochs. It also provides stacked limits for the two periods before and after the rebrightening divided at MJD 57260 and for the sum total of all observations. Flux conversions were determined using the HEASARC web tool WebPIMMS. The following constraints were used to compute the conversion factor between count rate and unabsorbed flux: 2.94×10^{10} weighted average nH (from HI Column Density Map of Dickey & Lockman 1990), photon index of 2 (Levan et al. 2013), and the 0.3-10 keV Swift XRT energy range. A conversion factor for count rate to unabsorbed flux was predicted at 3.854×10^{-11} ergs cm^{-2} s^{-1} per count s^{-1} .

2.2. Hubble Space Telescope Imaging Polarimetry

We requested Director’s Discretionary Time observations with the HST to obtain imaging polarimetry (#14348 PI: Yang). Our *HST* ACS/WFC multi-band imaging polarimetry of ASASSN-15lh occurred approximately $t_p=59$ days after the V -band maximum light.

The observations were taken with three different filters: F435W, F606W, and F775W. For the F435W filter, it was combined with one of the three UV polarized filters: POL0UV, POL60UV, and POL120UV. F606W and F775W were combined with one of the three visual polarized filters: POL0V, POL60V, and POL120V. Table 3 presents a log of the observations.

Multiple dithered exposures were taken in each observing configuration to allow for drizzling of the images. Bright stars and central regions of background galaxies in the field of view have been selected as an optimal input catalogue for image alignment through ‘`tweakreg`’

in `astrodizzle` (Gonzaga et al. 2012).

Aperture photometry was performed on the drizzled images for F435W, F606W, and F775W using an aperture radius of 10 pixels ($0.5''$). The local background level is estimated with a circular annulus of inner radius 20 pixels ($1.0''$) and outer radius 30 pixels ($1.5''$) around the source.

The calibration of the polarization data is described in more detail in Appendix A. The calculated polarization degree and angle for each filter are given in Table 3 and displayed in Figure 3. Not included in the errors are the calibration uncertainties (0.33% and 4 degrees for F435/POLUV and 0.24% and 5 degrees for F775W/POLV) from the standard deviation of the measurements of polarized standards as described in Appendix A.

2.3. Hubble Space Telescope Ultraviolet Spectroscopy

After ASASSN-15lh experienced a significant rebrightening at UV wavelengths, we also requested Director’s Discretionary Time observations to obtain a UV spectrum during the rebrightening (# 14450 PI: Brown). STIS observations using the G430L grism occurred on 2015 Dec 29 (see Table 4 for details). For these spectra we use the default HST reduction obtained from the Mikulski Archive for Space Telescopes (MAST;¹¹). We exclude any pixels flagged in the data quality array as well as two single-pixel spikes in the HST/STIS/CCD spectrum. We also obtained COS observations with the G140L grism with a central wavelength of 1105 Å. Four different wavelength positions were used. To improve the S/N from the default reduction, we extracted the spectrum with a smaller (17 pixel tall) extraction box. The four wavelength pointings were combined using a weighted average all pixels within a 0.5 Å bin. Because of the wavelength shift, both ends of the spectrum use progressively fewer of the pointings. The far blue end reaches ~ 1110 Å (though with low sensitivity at the end), while the net flux drops well below the noise before the red end is reached. Here it is trimmed at 1700 Å. The spectra are shown in Figure 4. Table 4 details the observation parameters and the rest-frame wavelengths covered by these observations.

¹¹ <https://archive.stsci.edu/hst/>

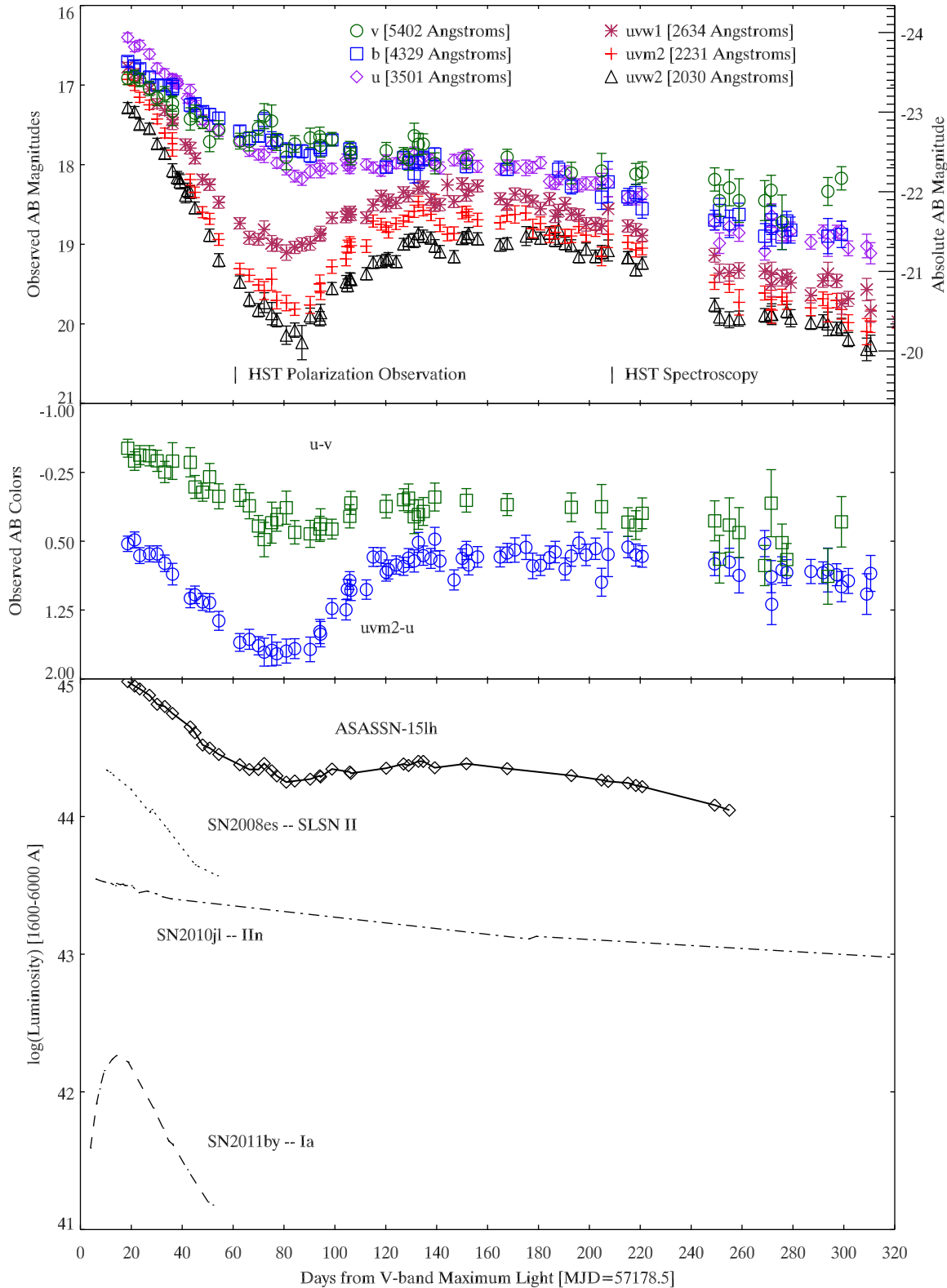


Figure 1. Top Panel: UVOT light curves of ASASSN-15lh in AB magnitudes. The right axis gives the absolute magnitude, which is calculated by subtracting a distance modulus of 40.34 from the observed magnitude. The late time rebrightening is brighter than the $m < -21$ cut-off for superluminous SNe (Gal-Yam 2012). Vertical lines indicate the epochs of the HST polarimetric and UV spectroscopic observations. The x-axis is given in days since the optical maximum (Dong et al. 2016a). Middle Panel: uvw2-u and u-v colors of ASASSN-15lh. The SN begins quite blue but reddens with time until the rebrightening during which the SN becomes bluer in the MUV-NUV. Bottom Panel: The integrated luminosity (in units of ergs s^{-1}) of ASASSN-15lh between 1600-6000 Å. Overplotted is the integrated luminosity of the SLSN II SN 2008es, which is of comparable brightness to the rebrightening event, as well as a bright SN IIIn and a normal SN Ia.

Table 1
Swift/UVOT Photometry of ASASSN-15lh

Name	Filter	MJD (days)	Mag	Mag Error	Upper Limit (mag)	Lower Limit (mag)	Rate (counts s ⁻¹)	Rate Error (counts s ⁻¹)
ASASSN-15lh	UVW2	57197.0974	15.555	0.066	20.993	11.085	5.371	0.327
ASASSN-15lh	UVW2	57199.7898	15.606	0.067	20.940	11.085	5.125	0.314
ASASSN-15lh	UVM2	57197.1005	15.240	0.062	20.358	10.555	4.405	0.252
ASASSN-15lh	UVM2	57199.7948	15.316	0.062	20.408	10.555	4.106	0.235
ASASSN-15lh	UVW1	57197.0939	15.265	0.060	20.519	11.145	7.410	0.408
ASASSN-15lh	UVW1	57199.7838	15.344	0.061	20.414	11.145	6.890	0.384
ASASSN-15lh	U	57197.0950	15.382	0.056	20.287	12.051	15.252	0.784
ASASSN-15lh	U	57199.7854	15.500	0.061	20.274	12.051	13.682	0.764
ASASSN-15lh	B	57197.0957	16.833	0.060	20.704	12.832	8.145	0.454
ASASSN-15lh	B	57199.7866	16.888	0.061	20.712	12.830	7.738	0.438
ASASSN-15lh	V	57197.0993	16.925	0.080	19.537	11.609	2.433	0.178
ASASSN-15lh	V	57199.7923	16.903	0.081	19.480	11.609	2.481	0.185

Note. — Magnitudes are given in the UVOT/Vega system for easier comparison with other SNe published in that system (see Brown et al. 2014 for a review). The three σ upper limits and lower (saturation) limits come from the exposure and background parameters. Most of the photometry of ASASSN-15lh is not close to either of these limits, but they are given for completeness and easy comparison with other SN photometry tables from the Swift Optical/Ultraviolet Supernova Archive (SOUSA; Brown et al. 2014). This table gives a portion of the data, while the full table will be available in machine readable format in the online version.

Table 2
0.3 - 10 keV X-ray 3 Sigma Upper limits

MJD (days)	Exposure (s)	Flux Limit (ergs cm ⁻² s ⁻¹)	Luminosity Limit (ergs s ⁻¹)
57197:57476	227634	1.118e-15	1.833e+41
57197:57283	53548	1.006e-14	1.650e+42
57283:57476	174086	6.257e-15	1.026e+42
57197.03	2484	1.024e-13	1.679e+43
57199.75	2354	1.432e-13	2.348e+43
57201.75	2267	1.122e-13	1.840e+43
57205.53	2874	1.171e-13	1.920e+43
57208.60	2854	8.912e-14	1.461e+43
57211.52	2667	9.538e-14	1.564e+43

Note. — The MJD column gives the start:stop range of dates for the coadded limits and the midpoint for the single observations. This table gives a portion of the data, while the full table will be available in machine readable format in the online version.

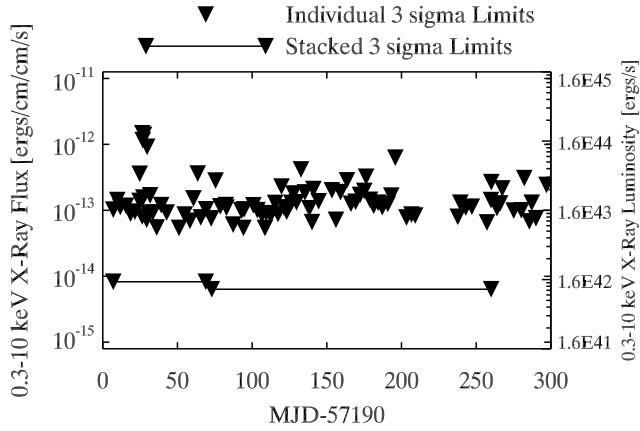


Figure 2. X-ray upper limits in the 0.3-10 keV range measured from Swift/XRT. Individual limits are shown as well as the coadded depths during the whole observation sequence, the initial peak, and the rebrightening episode.

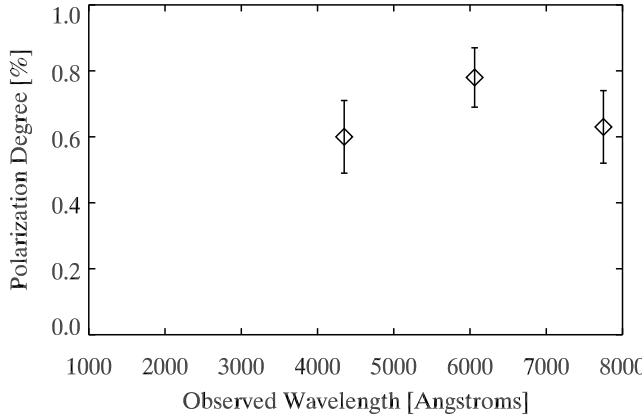


Figure 3. Wavelength dependence of the polarization measured with HST.

Table 3
HST Observations on 2015-08-03

ACS/WFC Filters	Polaroid	Date of Obs. UT	Exp. Time (seconds)	MAST Label Data Set	Polarization (%)	Position Angle Degrees
F435W	POL0UV	17:05:03	3×138	JCVH01040
	POL120UV	17:23:06	3×138	JCVH01050
	POL60UV	17:41:09	3×138	JCVH01060	0.60±0.11	23±5°
F606W	POL0V	15:32:13	3×122	JCVH01010
	POL120V	15:49:31	3×122	JCVH01020
	POL60V	16:06:46	3×122	JCVH01030	0.78±0.09	-11±3°
F775W	POL0V	18:35:27	3×137	JCVH01070
	POL120V	18:53:30	3×137	JCVH01080
	POL60V	19:11:30	3×137	JCVH01090	0.63±0.11	30±5°

Table 4
HST Spectroscopy from 2015 Dec 29

Start Time UT	Exposure seconds	Detector	Slit	Grism	Observed Range Angstroms	Rest-Frame Range Angstroms
18:01:07	434	STIS/CCD	52X0.1	G430L	2900-5700	2358-4634
18:14:56	1217	STIS/MAMA	52X0.1	G230L	1570-3180	1276-2585
19:27:43	2121	COS	PSA	G140L	1121-2148	911-1746

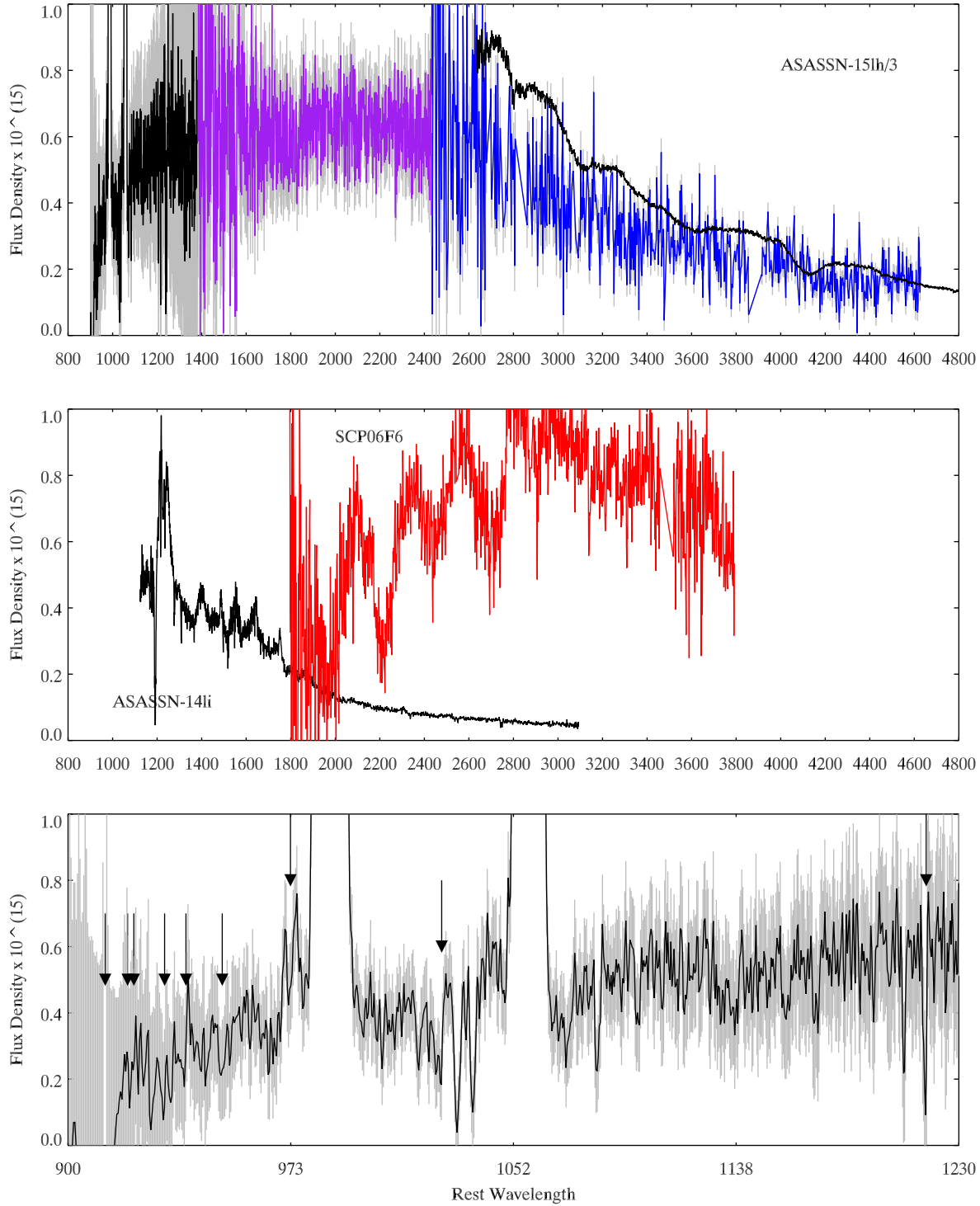


Figure 4. Top Panel: UV spectra of ASASSN-15lh during its rebrightening phase from COS and STIS (MJD 57386) along with an optical spectrum during its first peak (from SALT on MJD 57203, with flux scaled by a factor of 1/3; Dong et al. 2016a). The grey lines indicate the one sigma flux uncertainty. Middle Panel: For comparison we show spectra from SLSN SCP06F6 (VLT spectrum on MJD 53873; Barbary et al. 2009) and tidal disruption event ASASSN-14li (from HST on MJD 57034; Cenko et al. 2016). Bottom Panel: The COS FUV spectrum of ASASSN-15lh during the rebrightening is shown along with the positions of Lyman series transitions. The grey lines indicate the one sigma flux uncertainty.

3. RESULTS

3.1. Temporal Behavior

The ASAS V-band observations show the Swift observations began around the time of maximum light in the optical (Dong et al. 2016a). The Swift observations fade in all 6 filters, with the decay rate increasing to shorter wavelengths. This is shown in Figure 1. This wavelength-dependent fading and reddening continues to about 50 – 80 days after maximum light. At that point, the optical light curves begin fading more slowly and the UV light curves brighten. After 60 days of UV brightening, the *uvm2-u* colors are as blue as they were when Swift first began observing it. The absolute magnitudes are discussed in Dong et al. (2016a), with comparisons showing it to be the brightest SN ever discovered. The rebrightening is by itself as luminous in the UV as SLSNe. The rebrightening is not smooth, but exhibits possible flares or bumps. We note that this rebrightening appears quite different from the “double-peaked” SLSNe which exhibit an early time peak preceding the rise to the primary maximum Nicholl & Smartt (2016). While the rebrightening is obvious in the UV, it only manifests itself as a flattening in the optical decay rate and thus would not have been apparent without observer-frame UV observations. Thereafter the SN begins a slow decay in the optical, steeper in the UV filters. There may be an additional bump or leveling off in UVOT’s shortest wavelength *uvw2* filter at 260 days after maximum light.

To compute an integrated luminosity, we create an SED in as discussed in Brown et al. (2016, submitted). In summary, we begin the conversion from count rates to flux density at the Vega effective wavelengths using the average values from Poole et al. (2008). We linearly interpolate between the points and vary the flux density at the effective wavelength points until the spectrophotometric count rates from the SED match the observed count rates. Using the SEDs, we integrate the luminosity within the UVOT range (1600–6000 Å) and plot the luminosity evolution in the bottom panel of Figure 1. Also plotted is the integrated luminosity of the UV-bright SLSN II SN 2008es (Gezari et al. 2009). The late rebrightening of ASASSN-15lh is as bright as SN 2008es.

3.2. Geometry of the Explosion

The polarization degree is plotted as a function of wavelength in Figure 3. The flat polarization spectrum is inconsistent with that expected from interstellar dust in the Milky Way or the host galaxy. However, the shape of the polarization spectrum can vary depending on the dust properties. The Milky Way extinction along this line of sight is low, $A_V \sim 0.1$, and the internal extinction from the host galaxy is inferred to be low based on the very blue SED of ASASSN-15lh. An empirical upper bound of $9.0\% \text{ mag}^{-1} \times E(B-V)$ on interstellar polarization due to Milky Way dust was derived by Serkowski et al. (1975). For $A_V = 0.1$, we expect the degree of polarization due to Milky Way dust to be less than 0.29 %, which is smaller than the observed polarization. Most of the observed polarization is likely from the SN itself, but at the least the measured polarization represents an upper limit on the intrinsic polarization. The 0.6–0.8% polarization is high for a SN compared to e.g. Type Ia SNe (continuum or line polarization \leq

0.3% Wang & Wheeler 2008), but not that large, implying the emitting photosphere has a small asymmetry on the sky. It is comparable to that recently measured for the SLSN I LSQ14mo (Leloudas et al. 2015). It is also comparable to the core of SN IIP 2004dj (Leonard et al. 2006) Having only one epoch prevents us from measuring the time dependence and the change in shape as has been observed in suspected jet-driven SNe 2006aj and 2008D (Gorosabel et al. 2006; Maund et al. 2007, 2009; Gorosabel et al. 2010).

Broad-band polarimetry does not yield much detailed information on line polarization. The consistency of the polarization measurements suggests that the OII line (seen in absorption at ~ 4100 Å by Dong et al. 2016a and redshifted into the F606 filter bandpass), does not have a significantly higher polarization than the continuum which dominates the redder filters.

The geometry (or even the exact nature) of the energy injection from a magnetar is not often addressed. Bucciantini et al. (2009) used axisymmetric magnetohydrodynamic simulations to study the interaction. The formation of a polar jet is very asymmetric, yet for a GRB this jet punches through the SN explosion without transferring much energy. If a jet stalls early, one might also see roughly spherical ejecta from an intrinsically asymmetric explosion, provided the surrounding material is roughly spherical (Maund et al. 2009). (Soker 2016) suggests it is the jets themselves which power SLSNe. Such models should be explored further to determine the effect the jet might have on the observed luminosity and asphericity of the SN ejecta.

3.3. Early Spectral Shape

As apparent from the photometric colors and the SEDs created earlier, the spectrum rises strongly in the near-UV and then peaks in the *uvm2* filter (rest-frame wavelength 1800 Å). In the top panel of Figure 5 we show blackbody fits (in the rest-frame) using all six UVOT filters or just the three optical (*ubv*) filters for the first epoch. Since the conversion from observed count rates to flux density is spectrum dependent (Poole et al. 2008; Brown et al. 2010), we use the six-filter blackbody fit spectra to make the conversion for plotting purposes only. Using the hotter three-filter blackbody spectrum would reduce the *uvw1* flux density by 10% and the *u* flux by 5% because so many counts would be detected from blue edges of the filters. Neither blackbody fits the data well. The six-filter fit overestimates the optical and underestimates the UV flux. The extrapolation of the optical fit drastically overestimates the UV flux. Though line blanketing in the UV is much smaller than observed in radioactively-powered SNe (Quimby et al. 2011), line-blanketing depression of the UV flux is seen in hydrogen-dominated SNe II as the SN cools (e.g. Brown et al. 2007; Dessart et al. 2008). Thus determinations of the temperature using UV photometry can be incorrect (Valenti et al. 2016) and we give only estimates based on the observed spectral shape. We cannot tell from photometry alone whether the the early spectrum is a blackbody with UV absorption or what its origin is.

As the SN fades, the UV dominates the luminosity at all times, even at its reddest point during the flux minimum. Note that the magnitudes in Figure 1 are given

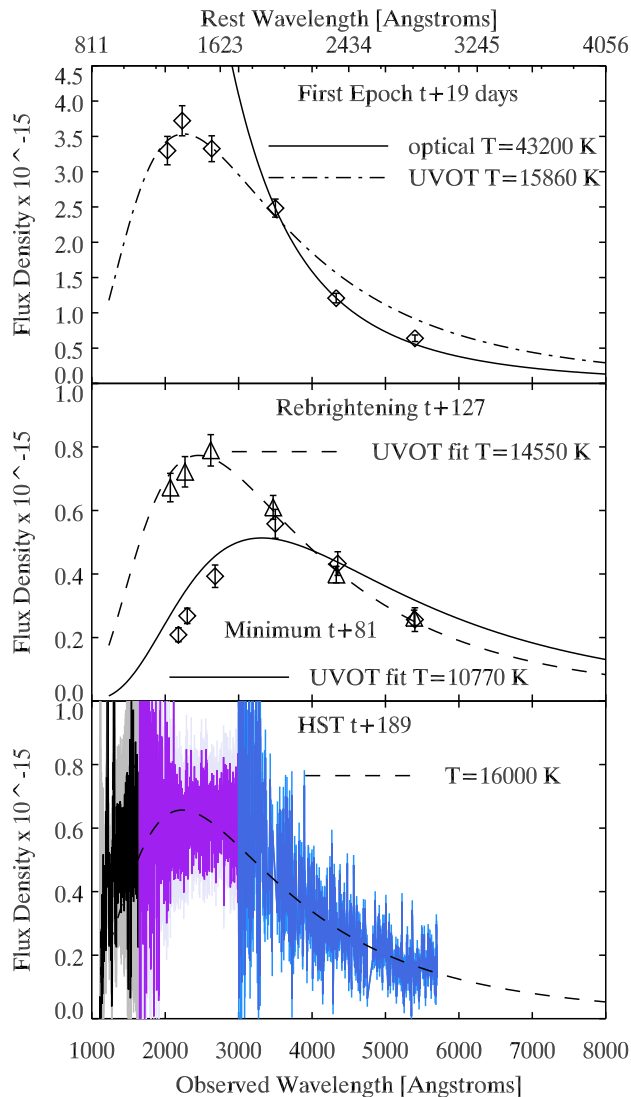


Figure 5. Top Panel: UVOT SEDs (in units of $\text{ergs s}^{-1} \text{cm}^{-2} \text{\AA}^{-1}$) from the first epoch (MJD=57197) compared to blackbody fits derived from the optical photometry (u,b,v; plotted with a solid line) and all six UVOT filters (plotted with a dotted-dashed line). The flux conversion is spectrum dependent—we plot the UVOT flux densities using conversion factors for the six-filter fit. Second Panel: SEDs from the light curve minimum (MJD=57259) and the first peak of the rebrightening (MJD=57305) compared to 6-filter blackbody fits. The flux conversions utilize the best-fit blackbody spectra. Bottom Panel: HST spectra from COS and STIS (MJD 57386) compared to a 16,000 K blackbody.

relative to the AB standard, which has a constant flux density in frequency, and thus a very blue spectral shape. Thus the colors still appear “red” or positive when comparing the UV to the optical. Best-fit blackbodies SEDs from the minimum and at the peak of the rebrightening are shown in the middle panel of Figure 5. The bottom panel of Figure 5 shows the HST spectra, confirming a similar spectral shape and showing that the UV luminosity comes from a hot continuum rather than line emission.

3.4. UV Spectrum During the Rebrightening

Our HST spectra of ASASSN-15lh during the rebrightening shows that the UV luminosity is dominated by a continuum rather than line emission. Compared to most SN spectra (see e.g. Filippenko 1997), the spectra appear featureless, at least lacking the broad absorption and emission lines usually seen. This is shown in Figure 4. The flux is dominated by a continuum broadly peaking at an observed wavelength of 2500 Å. The COS spectrum does show narrow hydrogen absorption from the Lyman series and a strong cutoff near that expected for the Lyman break. The spectra also feature other narrow absorption lines which will be discussed in Cooke et al. (2016, in preparation). Luminous, featureless spectra are ideal for the study of intervening interstellar, circumgalactic, and intergalactic material. Events like this will be very powerful tools to study the $z > 6$ universe as they are brighter than galaxies at that epoch.

3.5. X-Ray Limits

Because of the higher redshift, the X-ray limits (given in Table 2 and plotted in Figure 2) are not deep enough to have detected SNe comparable to relatively nearby circumstellar-interaction powered SNe II in which have been detected, such as SN 2005ip ($\sim 1.5 \times 10^{41} \text{ ergs s}^{-1}$; Katsuda et al. 2014), SN 2010jl ($\sim 10^{42} \text{ ergs s}^{-1}$; Ofek et al. 2014; Chandra et al. 2015), or SN 2006jd ($\sim 3 \times 10^{41} \text{ ergs s}^{-1}$; Chandra et al. 2012). Type IIP SNe are fainter than $\sim 10^{42} \text{ ergs s}^{-1}$ (Dwarkadas 2014). These limits are comparable to the limits placed on other SLSNe (e.g. Quimby et al. 2011). These limits are two orders of magnitudes more sensitive than the possible detection of SCP06F6 (Levan et al. 2013). Because of the high sampling it is unlikely that we missed a such a bright X-ray transient in ASASSN-15lh.

Metzger et al. (2015) predicted a late onset of X-ray emission ($L_X \sim 10^{42} - 10^{44}$) from an “ionization breakout.” We can exclude the bright end of this range with our well-sampled observations, and our summed limits rule out any long duration emission down to the low end of that range (see also Margutti 2015; Godoy-Rivera et al. 2016). Since ASASSN-15lh did not behave normally at late times in the optical/UV, that would also need to be taken into account in ruling out or creating new models.

4. DISCUSSION

4.1. The Nature of the Rebrightening

The unprecedented peak brightness was noted by Dong et al. (2016a) to pose problems for most supernova explosion models. The radioactive decay of ^{56}Ni is clearly ruled out (Kozyreva et al. 2016; Sukhbold & Woosley 2016). Theorists have risen to the challenge to explain how the peak brightness could be obtained, with a magnetar being the favored solution (Metzger et al. 2015; Bersten et al. 2016; Sukhbold & Woosley 2016; Dai et al. 2016) though Chatzopoulos et al. (2016) match the peak with models invoking only CSM interaction or with CSM interaction dominating the early phase.

In addition to its peak luminosity, ASASSN-15lh was also unusual in displaying a secondary peak in the UV light curve. Some models for the explosion of massive stars have qualitatively similar late-time peaks in the bolometric luminosity due to the radioactive decay of

^{56}Ni (Smidt et al. 2014, 2015), though Ni and other iron-peak elements in the ejecta would lead to strong line blanketing and a UV flux deficit. SLSN I iPTF13ehe also exhibited a late-time excess in the r-band which was accompanied by H-alpha emission from likely circumstellar interaction (Yan et al. 2015; Wang et al. 2015). Whether the excess was a flattening or a rebrightening is unclear due to the photometric sampling. Optical spectroscopy during the rebrightening of ASASSN-15lh does not show evidence of broad H-alpha (Milisavljevic et al. 2015) nor do we see strong or broad Lyman alpha emission in our UV spectra which would be expected from interaction with H-rich material. Some hydrogen may be present in the ejecta and/or interaction, but ionized because of the high temperatures (the narrow hydrogen absorption we see in Fig 4 could be farther out in an ejected shell or the host galaxy). The interaction could be with H-poor material, a model proposed for the luminous peaks of H-poor SLSNe I (Chatzopoulos & Wheeler 2012; Sorokina et al. 2015). Based on the velocity of a broad line in the early spectra (FWHM $\sim 10,000 \text{ km s}^{-1}$; Dong et al. 2016a) the start of the rebrightening would suggest material located about $8 \times 10^{15} \text{ cm}$ away, and the duration of the rise would suggest a radial extent of $4 \times 10^{15} \text{ cm}$. The details would be model dependent.

Recently, Chatzopoulos et al. (2016) proposed several hybrid models which could explain what they describe as a UV-bright plateau in the bolometric luminosity. They explain that primary peak and plateau as a combination of magnetar and circumstellar interaction. Reasonable fits to the whole bolometric light curve reproduce the early peak and late plateau with forward shock emission/magnetar and magnetar, respectively (labeled CSM0_A by Chatzopoulos et al. 2016), magnetar/forward shock and reverse shock emission (CSM0_B), forward shock and magnetar (CSM2_A), and forward shock and reverse shock from a pulsational pair-instability SN (CSM0). Some of these different scenarios from Chatzopoulos et al. (2016) can explain a flattening off, for example with a fading circumstellar interaction whose flux drops below that of a broad magnetar-powered bump. However, in all cases, the component resulting in the late-time plateau was significant at early times as well. Considering the UV light curves separate from the bolometric luminosity, however, provides an additional constraint pointing to distinct phases likely dominated by different mechanisms. The rapid UV fading followed by a rebrightening suggests the second component is turning on at late times, rather than just being revealed after the fading of the first component. Gilkis et al. (2015) suggest that late or prolonged accretion onto the remnant black hole could power such SLSNe in the jet feedback mechanism scenario.

The late-time UV spectra lack the broad features often seen in the rest-frame UV spectra of SLSNe (Barbary et al. 2009; Quimby et al. 2011) or even in the earlier optical spectra of ASASSN-15lh (Dong et al. 2016a). If magnetars are the correct interpretation for most SLSNe, then it is unlikely to explain the rebrightening phase for ASASSN-15lh. The difference in the early and late phases of ASASSN-15lh argues for different emission mechanisms.

4.2. A Tidal Disruption Event?

While we have focused our discussion on SLSN models (the preferred interpretation of Dong et al. 2016a due to spectroscopic comparisons with other SLSNe), the projected position of ASASSN-15lh coincides with the nucleus of the presumed host galaxy and shares some similarities with TDEs and theoretical predictions for such. Strubbe & Quataert (2009) show that a late-time flattening or even rebrightening can result from sub-Eddington fall-back accretion, though this has not been previously observed. Additionally, there are smaller scale chromatic and achromatic wiggles superimposed on the broad rebrightening which may be from density inhomogeneities in the circumstellar material (if the rebrightening is interaction driven), activity in a central engine, or irregularities in the accretion (if a TDE).

A TDE is a very asymmetric effect, with the emission thought to arise from the accretion disk itself or reprocessed by external material (see Holoien et al. 2016 for a discussion of the relevant distances for three TDEs observed with Swift). However, the expected or observed polarization signal from a TDE has not been well studied. Wiersema et al. (2012) report a $7.4 \pm 3.5\%$ linear polarization in Swift J164449.3+573451, but it is thought to be a beamed jet which outshines the light from the stellar disruption (Bloom et al. 2011; Burrows et al. 2011). If ASASSN-15lh is a TDE, the emitting region must have a small asymmetry on the sky to be consistent with our low measured polarization. While the required alignment might be rare, the exceptional characteristics of ASASSN-15lh do not encourage ruling out extreme (but allowed) parameters. The measured polarization does seem more like a supernova.

Compared to well-observed TDEs, ASASSN-15lh lacks the broad emission features often seen including hydrogen (Cenko et al. 2016; Arcavi et al. 2014), helium (Gezari et al. 2012; Holoien et al. 2016), and higher ionization emission lines (Cenko et al. 2016). Strubbe & Quataert (2011) predict a featureless optical/near-UV spectrum with absorption lines below 2000 \AA due to the high temperatures and low densities.

Dong et al. (2016a) and Godoy-Rivera et al. (2016) fit blackbody curves for the whole light curve of ASASSN-15lh and use the early cooling and expansion of the blackbody fits as an argument for a supernova event. The early temperatures, however, were extrapolated, as there were no multiwavelength data during the rise to maximum luminosity. Their blackbody fits show a cooling through the decline and then a strong reheating until ASASSN-15lh begins to fade again. The inferred radius rises slightly during the peak and decline and then drops during the rebrightening phase (Godoy-Rivera et al. 2016). This is interpreted to result from the photosphere receding as the outer layers expand and become optically thin. Godoy-Rivera et al. (2016) contrast the luminosity, radius, and temperature evolution with three well-observed TDEs to bolster the SLSN interpretation. However, ASASSN-15lh looks as different from SLSNe (e.g. Figures 5 and 6 from Inserra et al. 2013 and Figure 4 from Dong et al. 2016a) as it does from TDEs. In particular, the TDE ASASSN-14ae (Holoien et al. 2014) shows a cooling and reheating evolution qualitatively similar to ASASSN-

15lh and much different from the monotonic cooling seen in most SLSNe (Inserra et al. 2013). The large variety seen within SLSNe and TDEs make it hard to argue that ASASSN-15lh is an extreme example of one and rule out the other when it does not follow either very well.

4.3. Detectability at High Redshift

Because ASASSN-15lh had such a bright peak luminosity and remained bright for so long, it is of interest to know how far away such an object could be detected by current or future observatories. As noted in the introduction, SN explosions are tracers of star formation and SNe or TDEs could be used as backlights to study intervening systems in absorption. Because of their high luminosity and relatively featureless continua, SLSNe can be used as backlights to study the local environment, the host galaxy ISM, and circumgalactic medium and the IGM. These can then be studied in emission after the object fades. Estimating the brightness of objects at higher redshifts is often difficult because of the difference between the rest-frame and observer-frame wavelengths and the limited wavelength range of observations. The UV/optical observations of ASASSN-15lh, by covering shorter rest-frame (and observer-frame) wavelengths than usual ground-based observations, give us the amount of flux at those important wavelengths.

To predict the observability we use the SED (not the best fit blackbody spectra) from ASASSN-15lh from the first epoch as shown in Figure 5 as well as near the peak of the rebrightening. The observer-frame SED wavelengths are then shifted into the rest frame using a redshift of $z=0.2326$ (Dong et al. 2016a). The flux is increased by a factor of $1+z$ to account for flux dilution and scaled to a luminosity distance of 1171 Mpc (Dong et al. 2016a). This gives us a distance-corrected spectral energy distribution in the rest-frame. For a grid of redshift values, we then redshift this spectrum and correct for flux dilution and the luminosity distance (using `lumdist.pro`¹² with a standard cosmology with $H_0=70$, $\Lambda = 0.7$, $\Omega_m = 0.3$). We calculate spectrophotometry using these observer-frame SEDs based on filter curves from the Large Synoptic Survey Telescope (LSST) in the u, g, r, i, z, Y and UKIRT for J, H, K (Hewett et al. 2006) through the SNANA program (Kessler et al. 2009) with zeropoints computed on the AB system. The resulting curves of observed AB magnitudes as a function of redshift are displayed in Figure 6.

Although ASASSN-15lh is placed at increasing larger distances/redshifts, the shifting of the bright UV-flux into the observer-frame optical bandpasses keeps the magnitudes from dropping off as quickly. It would likely be detectable in the bluer optical bands to larger distances than shown, but we cut off at the observed short-wavelength edge of the UVOT observations and do not know how bright it is in the far-UV. Nevertheless, the redshifted mid-UV flux is detectable in r and i out to a redshift of $z\sim 4$ at the single visit depths of LSST. K -band observations down to $K_{AB} \sim 25$ would be able to detect it to $z\sim 12$. Tanaka et al. (2012) and Tanaka et al. (2013) did a similar study using theoretical models and SED matches to the SLSN II 2008es and also estimated rates as a function of redshift. Identifying these transients at

high redshifts would be complicated by the broad, time-dilated light curves, but there are multiple progenitor channels which are certainly bright enough. Regardless of the nature of ASASSN-15lh, high redshift counterparts would be useful backlights of intervening material. Using them to understand star formation or black hole evolution would require better ways of distinguishing SLSNe from TDEs.

5. SUMMARY

We have presented UV/optical photometry of ASASSN-15lh spanning nearly three hundred days from Swift/UVOT with only X-ray limits from XRT over the same period. We observe a remarkable UV rebrightening not seen in previous SLSNe or TDEs. We show from a single epoch of HST multi-band polarimetry that the emission region could have been only mildly asymmetric as projected on the sky. HST UV spectra during the rebrightening exhibit a lack of broad hydrogen emission (or any broad emission or absorption features) also dissimilar to SLSNe or TDEs. We demonstrated that the persistently strong UV flux could be detectable at high redshifts using already planned exposures with the LSST. By providing this unique UV, X-ray, and polarimetric data we hope to allow others to better constrain models for the progenitor system and explosion to determine more conclusively the nature of this enigmatic object. A successful model needs to result in a high UV/optical luminosity, low optical polarization, a UV-dominated rebrightening without H or He emission, and no bright X-rays.

We thank the HST director for approving the DDT requests. We thank Matt McMaster and Dean Hines for helping with the calibration of the ACS/WFC polarizers. Based on observations made with the NASA/ESA Hubble Space Telescope, obtained from the data archive at the Space Telescope Science Institute. STScI is operated by the Association of Universities for Research in Astronomy, Inc. under NASA contract NASA 5-26555. These observations are associated with programs #14348 and #14450. Support for this work was provided by NASA through grant number HST-GO-14450.001-A from the Space Telescope Science Institute, which is operated by AURA, Inc., under NASA contract NAS 5-26555. JCW was supported by STScI by STScI grant HST-AR-13276.02-A. This work is supported by the Swift GI program through grant NNX15AR41G. The Swift Optical/Ultraviolet Supernova Archive (SOUSA) is supported by NASA's Astrophysics Data Analysis Program through grant NNX13AF35G. This work made use of public data in the *Swift* data archive from observations requested by several others (PIs: Dong, Godoy, Holoien, Leloudas, Jonker). This research has made use of NASA's Astrophysics Data System Bibliographic Services.

REFERENCES

- Arcavi, I., Gal-Yam, A., Sullivan, M., et al. 2014, *ApJ*, 793, 38
 Barbary, K., Dawson, K. S., Tokita, K., et al. 2009, *ApJ*, 690, 1358
 Berger, E., Chornock, R., Lunnan, R., et al. 2012, *ApJ*, 755, L29

¹² <http://idlastro.gsfc.nasa.gov/ftp/pro/astro/lumdist.pro>

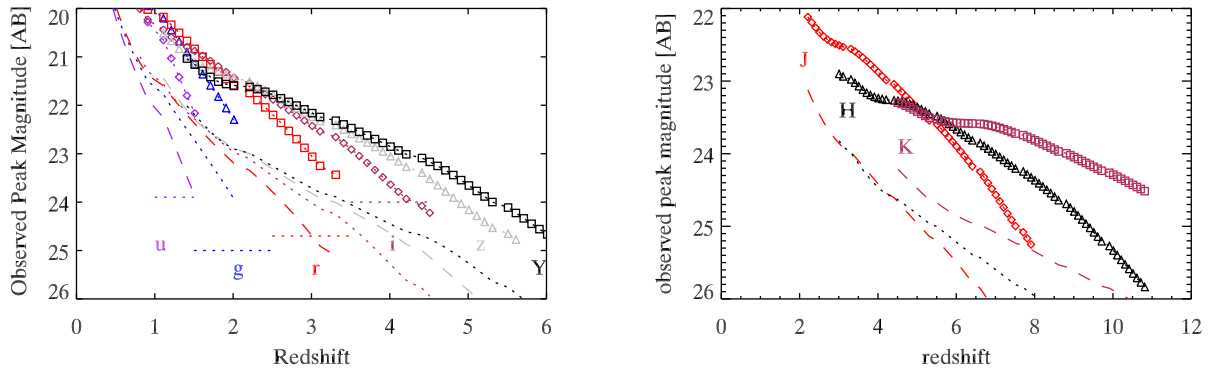


Figure 6. Left Panel: Predicted observed magnitudes (in the LSST filter system) for ASASSN-15lh near peak (symbols) and during the rebrightening (dashed and dotted lines) if it were observed at different redshifts. The high UV luminosity is redshifted into the optical bands and detectable to redshifts of $z \sim 4$ with LSST in single visits. This includes just the contribution observed by UVOT (rest frame 1300-4900 Å). Right Panel: Predicted observed peak magnitudes of the ASASSN-15lh SED near peak (symbols) and during the rebrightening (dashed and dotted lines) redshifted into the NIR.

- Bersten, M. C., Benvenuto, O. G., Orellana, M., & Nomoto, K. 2016, *ApJ*, 817, L8
- Biretta, J., Kozhurina-Platais, V., Boffi, F., Sparks, W., & Walsh, J. 2004, *ACS Polarization Calibration - I. Introduction and Status Report*, Tech. rep.
- Bjorkman, K. S. 1994, *Ap&SS*, 221, 335
- Bloom, J. S., Giannios, D., Metzger, B. D., et al. 2011, *Science*, 333, 203
- Breeveld, A. A., Landsman, W., Holland, S. T., et al. 2011, in *American Institute of Physics Conference Series*, Vol. 1358, *GAMMA RAY BURSTS 2010. AIP Conference Proceedings*, ed. J. E. McEnery, J. L. Racusin, & N. Gehrels, 373–376
- Brown, P. J., Breeveld, A. A., Holland, S., Kuin, P., & Pritchard, T. 2014, *A&SS*, 354, 89
- Brown, P. J., Dessart, L., Holland, S. T., et al. 2007, *ApJ*, 659, 1488
- Brown, P. J., Roming, P. W. A., Milne, P., et al. 2010, *ApJ*, 721, 1608
- Bucciantini, N., Quataert, E., Metzger, B. D., et al. 2009, *MNRAS*, 396, 2038
- Burrows, D. N., Hill, J. E., Nousek, J. A., et al. 2005, *Space Science Reviews*, 120, 165
- Burrows, D. N., Kennea, J. A., Ghisellini, G., et al. 2011, *Nature*, 476, 421
- Cenko, S. B., Cucchiara, A., Roth, N., et al. 2016, *ApJ*, 818, L32
- Chandra, P., Chevalier, R. A., Chugai, N., et al. 2012, *ApJ*, 755, 110
- Chandra, P., Chevalier, R. A., Chugai, N., Fransson, C., & Soderberg, A. M. 2015, *ApJ*, 810, 32
- Chatzopoulos, E., & Wheeler, J. C. 2012, *ApJ*, 760, 154
- Chatzopoulos, E., Wheeler, J. C., Vinko, J., Horvath, Z. L., & Nagy, A. 2013, *ApJ*, 773, 76
- Chatzopoulos, E., Wheeler, J. C., Vinko, J., et al. 2016, *ArXiv e-prints*, arXiv:1603.06926
- . 2011, *ApJ*, 729, 143
- Chomiuk, L., Chornock, R., Soderberg, A. M., et al. 2011, *ApJ*, 743, 114
- Cooke, J., Sullivan, M., Gal-Yam, A., et al. 2012, *Nature*, 491, 228
- Cracraft, M., & Sparks, W. B. 2007, *ACS Polarization Calibration - Data, Throughput, and Multidrizze Weighting Schemes*, Tech. rep.
- Dai, Z. G., Wang, S. Q., Wang, J. S., Wang, L. J., & Yu, Y. W. 2016, *ApJ*, 817, 132
- Dessart, L., Hillier, D. J., Waldman, R., Livne, E., & Blondin, S. 2012, *MNRAS*, 426, L76
- Dessart, L., Blondin, S., Brown, P. J., et al. 2008, *ApJ*, 675, 644
- Dickey, J. M., & Lockman, F. J. 1990, *ARAA*, 28, 215
- Dong, S., Shappee, B. J., Prieto, J. L., et al. 2015, *The Astronomer's Telegram*, 7774, 1
- . 2016a, *Science*, 351, 257
- . 2016b, *Science*, 351, 257
- Dwarkadas, V. V. 2014, *MNRAS*, 440, 1917
- Filippenko, A. V. 1997, *ARAA*, 35, 309
- Gal-Yam, A. 2012, *Science*, 337, 927
- Gal-Yam, A., Mazzali, P., Ofek, E. O., et al. 2009, *Nature*, 462, 624
- Gezari, S., Halpern, J. P., Grupe, D., et al. 2009, *ApJ*, 690, 1313
- Gezari, S., Chornock, R., Rest, A., et al. 2012, *Nature*, 485, 217
- Gilkis, A., Soker, N., & Papish, O. 2015, *ArXiv e-prints*, arXiv:1511.01471
- Godoy-Rivera, D., Stanek, K. Z., Kochanek, C. S., et al. 2016, *ArXiv e-prints*, arXiv:1605.00645
- Gonzaga, S., Hack, W., Fruchter, A., & Mack, J. 2012, *The DrizzlePac Handbook*
- Gorosabel, J., Larionov, V., Castro-Tirado, A. J., et al. 2006, *A&A*, 459, L33
- Gorosabel, J., de Ugarte Postigo, A., Castro-Tirado, A. J., et al. 2010, *A&A*, 522, A14
- Hewett, P. C., Warren, S. J., Leggett, S. K., & Hodgkin, S. T. 2006, *MNRAS*, 367, 454
- Holoien, T. W.-S., Prieto, J. L., Bersier, D., et al. 2014, *MNRAS*, 445, 3263
- Holoien, T. W.-S., Kochanek, C. S., Prieto, J. L., et al. 2016, *ArXiv e-prints*, arXiv:1602.01088
- Insera, C., Smartt, S. J., Jerkstrand, A., et al. 2013, *ApJ*, 770, 128
- Kasen, D., & Bildsten, L. 2010, *ApJ*, 717, 245
- Katsuda, S., Maeda, K., Nozawa, T., Pooley, D., & Immler, S. 2014, *ApJ*, 780, 184
- Kessler, R., Bernstein, J. P., Cinabro, D., et al. 2009, *PASP*, 121, 1028
- Kozyreva, A., Blinnikov, S., Langer, N., & Yoon, S.-C. 2014, *A&A*, 565, A70
- Kozyreva, A., Hirschi, R., Blinnikov, S., & den Hartogh, J. 2016, *MNRAS*, arXiv:1603.00335
- Kraft, R. P., Burrows, D. N., & Nousek, J. A. 1991, *ApJ*, 374, 344
- Leloudas, G., Chatzopoulos, E., Dilday, B., et al. 2012, *A&A*, 541, A129
- Leloudas, G., Patat, F., Maund, J. R., et al. 2015, *ArXiv e-prints*, arXiv:1511.04522
- Leonard, D. C., Filippenko, A. V., Ganeshalingam, M., et al. 2006, *Nature*, 440, 505
- Levan, A. J., Read, A. M., Metzger, B. D., Wheatley, P. J., & Tanvir, N. R. 2013, *ApJ*, 771, 136
- Loeb, A., & Ulmer, A. 1997, *ApJ*, 489, 573
- Margutti, R. 2015, *The Astronomer's Telegram*, 8089, 1
- Maund, J. R., Wheeler, J. C., Baade, D., et al. 2009, *ApJ*, 705, 1139
- Maund, J. R., Wheeler, J. C., Patat, F., et al. 2007, *A&A*, 475, L1
- Metzger, B. D., Margalit, B., Kasen, D., & Quataert, E. 2015, *MNRAS*, 454, 3311
- Milislavljevic, D., James, D. J., Marshall, J. L., et al. 2015, *The Astronomer's Telegram*, 8216, 1
- Montier, L., Plaszczyński, S., Levrier, F., et al. 2015, *A&A*, 574, A135

- Moretti, A., Campana, S., Mineo, T., et al. 2005, in Proc. SPIE, Vol. 5898, UV, X-Ray, and Gamma-Ray Space Instrumentation for Astronomy XIV, ed. O. H. W. Siegmund, 360–368
- Muzzio, J. C., & Orsatti, A. M. 1977, AJ, 82, 474
- Naghizadeh-Khouei, J., & Clarke, D. 1993, A&A, 274, 968
- Nicholl, M., & Smartt, S. J. 2016, MNRAS, 457, L79
- Nicholl, M., Smartt, S. J., Jerkstrand, A., et al. 2013, Nature, 502, 346
- . 2014, MNRAS, 444, 2096
- Nicholls, B., Holoiën, T. W.-S., Stanek, K. Z., et al. 2015, The Astronomer’s Telegram, 7642, 1
- Ofek, E. O., Zoglauer, A., Boggs, S. E., et al. 2014, ApJ, 781, 42
- Pastorello, A., Smartt, S. J., Botticella, M. T., et al. 2010, ApJL, 724, L16
- Poole, T. S., Breeveld, A. A., Page, M. J., et al. 2008, MNRAS, 383, 627
- Quimby, R. M., Wheeler, J. C., Höflich, P., et al. 2007, ApJ, 666, 1093
- Quimby, R. M., Kulkarni, S. R., Kasliwal, M. M., et al. 2011, Nature, 474, 487
- Rees, M. J. 1988, Nature, 333, 523
- Riess, A. G., Strolger, L.-G., Tonry, J., et al. 2004, ApJL, 600, L163
- Roming, P. W. A., Kennedy, T. E., Mason, K. O., et al. 2005, Space Science Reviews, 120, 95
- Serkowski, K. 1958, Acta Astronomica, 8, 135
- Serkowski, K. 1962, Advances in Astronomy and Astrophysics, 1, 289
- Serkowski, K., Mathewson, D. S., & Ford, V. L. 1975, ApJ, 196, 261
- Sirianni, M., Jee, M. J., Benítez, N., et al. 2005, PASP, 117, 1049
- Smidt, J., Whalen, D. J., Chatzopoulos, E., et al. 2015, ApJ, 805, 44
- Smidt, J., Whalen, D. J., Wiggins, B. K., et al. 2014, ApJ, 797, 97
- Smith, N., Li, W., Foley, R. J., et al. 2007, ApJ, 666, 1116
- Soker, N. 2016, New Astronomy, 47, 88
- Sorokina, E., Blinnikov, S., Nomoto, K., Quimby, R., & Tolstov, A. 2015, ArXiv e-prints, arXiv:1510.00834
- Sparks, W. B., & Axon, D. J. 1999, PASP, 111, 1298
- Sparks, W. B., Bond, H. E., Cracraft, M., et al. 2008, AJ, 135, 605
- Strubbe, L. E., & Quataert, E. 2009, MNRAS, 400, 2070
- . 2011, MNRAS, 415, 168
- Sukhbold, T., & Woosley, S. 2016, ArXiv e-prints, arXiv:1602.04865
- Tanaka, M., Moriya, T. J., & Yoshida, N. 2013, MNRAS, 435, 2483
- Tanaka, M., Moriya, T. J., Yoshida, N., & Nomoto, K. 2012, MNRAS, 422, 2675
- Valenti, S., Howell, D. A., Stritzinger, M. D., et al. 2016, MNRAS, arXiv:1603.08953
- Wang, L., & Wheeler, J. C. 2008, ARAA, 46, 433
- Wang, S. Q., Liu, L. D., Dai, Z. G., Wang, L. J., & Wu, X. F. 2015, ArXiv e-prints, arXiv:1509.05543
- Whittet, D. C. B., Martin, P. G., Hough, J. H., et al. 1992, ApJ, 386, 562
- Wiersema, K., van der Horst, A. J., Levan, A. J., et al. 2012, MNRAS, 421, 1942
- Woosley, S. E. 2010, ApJ, 719, L204
- Yan, L., Quimby, R., Ofek, E., et al. 2015, ArXiv e-prints, arXiv:1508.04420

APPENDIX

Computing the degree and orientation of linear polarization

The Stokes vectors and associated errors were calculated by following the case of three polarizers described by Sparks & Axon (1999). Neither the ACS visible or UV polarizers are ideal. Significant instrumental polarization likely comes from the M3 and IM3 mirrors (Biretta et al. 2004). Correction factors $C(CCD, POLnXX, spectral\ filter, n)$ in equation 1 are applied and investigated in different calibration proposals: 9586 (P.I. W.B. Sparks), 9661 & 10055 (P.I. J. Biretta), and 13964 (P.I. M. McMaster). These included observations of unpolarized and polarized stars.

HRC has been unavailable since January 2007, and all the observations and involved calibrations in the most recent polarimetric calibration proposal 13964 are only for the usage of WFC. The polarimetry measurements for the same targets reproduced from the on-orbit calibration runs vary on the order of $1 \sim 2\%$, which is most likely due to instrumental effects at the $1 - 2\%$ level and a few degrees in the position angle (Sparks et al. 2008). Importantly, the optical chain containing WFC with the filters F435W/POLUV has never been calibrated before. By applying correction factors to each combination of wavelength filter and polarization filter sets (Cracraft & Sparks 2007), one can correct the throughput for each polarizer, thus removing the instrumental polarization to obtain the true polarized level of the source. Correction factors for F606W/POLV have been well characterized by Cracraft & Sparks (2007) and reach a precision down to $\sigma_P\% \approx 0.3\%$ and $\sigma_\theta \sim 3^\circ$. The correction factors for F775W/POLV have not been tested by any other observations until program 13964.

We calibrated the throughput of F435W/POLUV and F775W/POLV filter sets based on the most recent calibration program 13964. The correction factors reproduce the polarization degrees of the polarized standard: Vela1-81 measured from the observations 13964 are: $5.89 \pm 0.09\%$, $6.02 \pm 0.09\%$, $5.40 \pm 0.09\%$ among three rolling angles, for a mean of 5.77% for F435W, compared to the published value 6.1% (Whittet et al. 1992). The measured position angles are 6° , 1° , -2° , compared to a published value 1° (Whittet et al. 1992). Measurements of the unpolarized standard EGGR-247 give the polarization degree to be $0.70 \pm 0.02\%$ for F435/POLUV.

For F775W/POLV, we get $5.42 \pm 0.07\%$, $5.10 \pm 0.07\%$, $5.14 \pm 0.07\%$, for a mean of 5.21% compared to the published value 6.29% (Whittet et al. 1992). The position angles are 4° , 3° , and 8° , compared to -1° (Whittet et al. 1992). The measurement on EGGR-247 gives the polarization degree $0.38 \pm 0.07\%$. The correction factors for F775W/POLV listed in Table 1 from Cracraft & Sparks (2007) reproduce: $6.12 \pm 0.07\%$, $4.47 \pm 0.07\%$, $5.04 \pm 0.07\%$ among the three roll angles, for a mean of 5.21% compared to the published value 6.29% (Whittet et al. 1992).

We found that the previously published correction factors for F775W/POLV (Whittet et al. 1992) fail to produce consistent degree of polarizations among the observations of the same polarized standard with three different roll angles. Moreover, the mean level of the polarization degree for Vela1-81 is measured to have decreased by $\sim 1.1\%$. Vela1-81 is an OB star (Muzzio & Orsatti 1977), and the most recent published polarimetry measurement is from 1987 (Whittet et al. 1992). Because many OB stars, especially OB supergiants and Be stars are polarimetric variables

Table 5
Count Rate Ratios used as Correction Factors

Band	POL60/POL0	POL120/POL0
F435W/POLUV	1.0266	0.9734
F606W/POLV	0.979	1.014
F775W/POLV	0.9788	0.9959

(Bjorkman 1994), we cannot exclude the possibility that the degree of polarization of OB supergiant Vela181 has changed in the last three decades.

Our calibration reproduced the polarization to be consistent among the three roll angles, with uncertainties: $\sigma_F\% \approx 0.33\%$ and $\sigma_\theta \sim 4^\circ$ for F435W/POLUV, $\sigma_F\% \approx 0.24\%$ and $\sigma_\theta \sim 5^\circ$ for F775W/POLV. Since F606W/POLV has been done at a single roll angle in 13964, and which has been tested by other observing runs, we use the correction factors for F606W/POLV listed in Cracraft & Sparks (2007). Table 5 shows the correction factors we used as follows:

$$r(n) = C(\text{CCD}, \text{POL}n\text{XX}, \text{spectral filter}, n) r_{\text{obs}}(n)' \quad (1)$$

Stokes vectors in the different bands are computed for the target using the following equations.

$$\begin{aligned} I &= \left(\frac{2}{3}\right)[r(0) + r(60) + r(120)] \\ Q &= \left(\frac{2}{3}\right)[2r(0) - r(60) - r(120)] \\ U &= \left(\frac{2}{\sqrt{3}}\right)[r(60) - r(120)] \end{aligned}$$

The cross-polarization leakage is insignificant for POLVIS filters (Biretta et al. 2004). Then F% is calculated using the Stokes vectors. These corrections together with the calibration of the source count rates vectorially remove the instrumental polarization of the WFC. The position angle (P.A.) is calculated using the Stokes vectors and the roll angle of the *HST* spacecraft (PA_V3 in the data headers) as shown in Equation 3. Another parameter, χ , containing information about the camera geometry which is derived from the design specification, has also been corrected. For the WFC, $\chi = -38.2^\circ$. The degree of polarization of ASASSN-15lh at $t_p=59$ days after the V-band maximum light is shown in Table 3.

$$p\% = \frac{\sqrt{Q^2 + U^2}}{I} \times \frac{T_{\text{par}} + T_{\text{perp}}}{T_{\text{par}} - T_{\text{perp}}} \times 100\% \quad (2)$$

$$\text{P.A.} = \frac{1}{2} \tan^{-1} \left(\frac{U}{Q} \right) + \text{PA.V3} + \chi \quad (3)$$

The classical method proposed by Serkowski (1958) and Serkowski (1962) is often used for the determinations of the polarization and associated uncertainties. Montier et al. (2015) investigated the statistical behavior of basic polarization fraction and angle measurements. Asymmetrical terms and correlations in the covariance matrix have been included (compare to classical determinations discussed by Naghizadeh-Khouei & Clarke (1993)). We use Equation 4 and Equation 5 to describe the uncertainty of $p\%$ and P.A. The detailed derivation has been provided in Appendix F of Montier et al. (2015).

$$\sigma_p^2 = \frac{1}{p^2 I^4} \times (Q^2 \sigma_Q^2 + U^2 \sigma_U^2 + p^4 I^2 \sigma_I^2 + 2QU \sigma_{QU} - 2IQ p^2 \sigma_{IQ} - 2IU p^2 \sigma_{IU}) \quad (4)$$

$$\sigma_{\text{P.A.}} = \sqrt{\frac{Q^2 \sigma_U^2 + U^2 \sigma_Q^2 - 2QU \sigma_{QU}}{Q^2 \sigma_Q^2 + U^2 \sigma_U^2 + 2QU \sigma_{QU}}} \times \frac{\sigma_p}{2p} \text{ rad} \quad (5)$$

The Stokes I vector gives the total intensity of the source. The magnitudes of the SN were obtained by applying the ACS/WFC zeropoint correction. The aperture corrections calculated with the ACS/WFC encircled energy profile for each bandpass has also been done according to Sirianni et al. (2005).